Ceramics International 47 (2021) 14311–14319

Contents lists available at ScienceDirect

Ceramics International

journal homepage: www.elsevier.com/locate/ceramint

Numerical Analysis of stress evolution in thermal barrier coating system during two-stage growth of heterogeneous oxide

Pengfei Liu [a], Peng Jiang [a], Yongle Sun [b], Rong Xu [c], Tiejun Wang [a], Weixu Zhang [a,*]

[a] State Key Laboratory for Strength and Vibration of Mechanical Structures, School of Aerospace Engineering, Xi'an Jiaotong University, Xi'an, Shaanxi, 710049, China
[b] School of Mechanical, Aerospace and Civil Engineering, The University of Manchester, Sackville Street, Manchester, M13 9PL, UK
[c] School of Mechanical Engineering, Purdue University, West Lafayette, IN, 47907, USA

ARTICLE INFO

Keywords:
Thermal barrier coating (TBC) system
Thermally grown oxide (TGO)
Mixed oxide (MO)
Stress evolution

ABSTRACT

The mechanical stability of the thermal barrier coating (TBC) systems is important for the heavy-duty gas turbine during operation and maintenance. The growth of thermally grown oxide (TGO), which controls the mechanical stability of TBC systems, usually consists of two stages. In the first stage, the outer mixed oxide (MO) and alumina grow simultaneously. In the second stage, the intact alumina protective layer is gradually replaced by the porous inner MO. The MO deteriorates the interface integrity and exhibits a higher growth rate, which should be investigated. In this study, a numerical method was developed to simulate the stress evolution of two-stage TGO growth. The results show that the inner MO growth can significantly change the stress evolution during high-temperature oxidation and induce higher thermal mismatch stress after cooling down. This adverse effect enhances the risk of TC failure and should be taken seriously in the heavy-duty gas turbine's operation and maintenance.

1. Introduction

The heavy-duty gas turbine is subjected to a long period of high-temperature operation during service. Thermal barrier coating (TBC) systems are widely used to provide thermal protection for superalloy blades [1–4]. A typical TBC system consists of a yttria-partially stabilized zirconia top coat (TC) and aluminium-rich bond coat (BC). Upon exposure to high temperatures, a heterogeneous thermally grown oxide (TGO) layer forms at the interface between the TC and BC. Regular maintenance inspections are necessary for heavy-duty gas turbines. Prior to an inspection, a force cooling practice is performed to speed the cool-down process and shorten the outage time [5]. Accompanied by the cool-down process, the thermal mismatch stress is generated. The growth of the TGO layer will not only induce high local stresses during operation but also intensify the mismatch stress after cooling down [6–10]. These stresses may lead to the formation of undesirable microcracks or macrocracks. The nucleation and coalescence of cracks at the TGO–TC interface within the TGO or at the TGO–BC interface causes the delamination or spalling of the protective TC, leading to the catastrophic failure of the TBC system and the superalloy blades of gas turbines [10–14]. Although the mechanical degradation caused by the TGO growth has been experimentally confirmed [6–9,15–18], the impact of TGO growth on the evolution of stresses remains unclear. In particular, the stress fields within the heterogeneous TGO and TC layers are complex, rendering the experimental characterization of the oxidational–mechanical behaviors of the TBC system an exigent task [19–25]. An accurate analysis is imperative for understanding the stress evolution and failure induced by TGO growth.

In order to achieve a well-predicted stress evolution, the description of the TGO growth process should be consistent with the experimental observation. In most of the previous numerical models [26–47], a simplification was used in which the TGO only consists of a single component (i.e., alumina). However, according to experimental reports, the realistic description of the TGO layer should consider not only the growth of alumina, but also the formation of multiple mixed oxides (MO), such as chromia, spinel, and nickel oxide [8,48–52]. Niranatlumpong et al. confirmed that the TGO contains three different oxide layers [53]. From top to bottom, these are Ni, Cr-rich oxide layer (i.e., outer MO), alumina scale layer, and Cr, Al, and Ni-rich oxide layers (i.e., inner MO). The detailed description of TGO growth behavior has been experimentally studied by Bai et al. [54]. As shown in Fig. 1, the TGO growth could be divided into two stages: in the first stage (i.e., 0–200 h), the outer MO and dense alumina grow simultaneously; in the second stage (i.e., after 200 h), the MO formed gradually from the

* Corresponding author.
E-mail address: zhangwx@mail.xjtu.edu.cn (W. Zhang).

https://doi.org/10.1016/j.ceramint.2021.01.292
Received 19 November 2020; Received in revised form 13 January 2021; Accepted 30 January 2021
Available online 5 February 2021

bottom of the Al_2O_3 layer. Due to the depletion of aluminum within the region near the Al_2O_3 layer, the Al_2O_3 phase would transform to (Ni, Co) Al_2O_4 spine, i.e. the inner MO [54]. The growth of the inner MO swallowed the previously formed Al_2O_3, leading to the disappearance of the dense Al_2O_3 scale. Similar observations have also been reported by other researchers [16,52,55–57]. The mechanical stability of porous MO is considerably lower than that of dense alumina, and the growth rate of MO is several times higher than that of alumina [58]. Hence, the formation and continuous growth of MO during the second stage is expected to significantly influence the performance and service life of the TBC system.

Motivated by the experimental observations, a few recent works have studied the stress evolution and mechanical degradation by considering the growth of both MO and alumina layers. Xu et al. investigated the interfacial failure mechanism by considering the role of mixed oxides [59] and concluded that the high growth rate of MO induces the initiation and propagation of interface cracks. Lv et al. introduced a thermo–elasto–viscoplastic constitutive model in which both the sintering and MO growth effects were considered [60]. Busso et al. investigated the results of MO oxidation under stresses with different levels of bond coat roughness [61]. The FE modeling demonstrated that the MO growth generated a four-time higher out-of-plane tensile stress within the yttria stabilized zirconia (YSZ) at high temperature. Xie et al. set up a spherical model to describe the growth of MO and studied the corresponding catastrophic stress [62]. The spherical model can provide an understanding of the first-order effect of MO growth, but the model is oversimplified and cannot capture the real TGO composition evolution. Overall, the aforementioned studies only focused on the situation in which the MO formed above the alumina layer (i.e., the first stage of TGO growth). The second stage of oxidation (i.e., the inner MO forms underneath the alumina layer, rises upward, and eventually replaces the alumina) is usually neglected. Moreover, as aforementioned, the TBC system suffers from high thermal mismatch stress due to the cool-down process. The influence of inner MO growth on the stress after cooling down is of great importance to the mechanical stability of the TBC system during maintenance. However, the problem has received scant attention in the research literature. Under these circumstances, the evolution analysis of the stress field and prediction of the crack formation would considerably differ from the more realistic results yielded by a two-stage TGO oxidation model. Hence, the variation between the qualitative results obtained by numerical studies and experimental observations is probably due to neglecting the inner MO growth [39,47,63–70]. Previous studies show that the detailed microstructure of TGO dominates the failure of TBC. However, up to date, there is no general and accurate method to analyze the stress evolution of the two-stage growth of TGO.

In the present work, a numerical method and a new accurate TGO-growth model that can well represent the two stages of oxidation are formulated. The growth of the inner MO is introduced into the new model by adding a material 'phase' transition from alumina to MO at the bottom of the TGO layer. The TGO-growth model is implemented into the finite element simulation by utilizing the user subroutines UEXPAN and USDFLD in ABAQUS. During the high-temperature oxidation stage and rapid-cooling stage, the evolution of the stress field within the TC layer and at the BC–TGO–TC interfaces in the TBC system were well predicted. The predicted stress distributions in the two cases with and without considering the growth of the inner MO at high-temperature oxidation were compared. The growth of the inner MO significantly increased the thermal growth stress within the TC layer and at the interfaces. The influence of the TGO layer creep on the stress evolution was also investigated. It was found that the stress field considerably depended on the creep behavior of the TGO layer, i.e., the high creep rate moderated the stress generated during the oxidation. Although the stress generated at high temperature can be released due to creep, the growth of MO can still aggravate the thermal mismatch stress after cooling down. This prediction of oxidation-induced stress evolution can aid in better comprehending the mechanical failure of the TBC system and designing a TBC system with enhanced mechanical stability.

2. Numerical analysis

2.1. TGO growth

The TGO usually exhibits a columnar grain microstructure, as shown in Fig. 2. The non-mechanical strain associated with the TGO growth contains two components: the thickening strain (ε_t) and lateral strain (ε_l) related to the TGO's formed at the TGO–BC interface and inside the oxide layer, respectively. The directions of ε_t and ε_l are normal and parallel to the interface, respectively. The oxidation of aluminium is presented by the following reaction:

$$4Al + 3O_2 \rightarrow 2Al_2O_3 \quad (1)$$

The $\varepsilon_l^{Al_2O_3}$, which is the lateral strain associated with the formation of Al_2O_3, varies within the experimentally determined range, i.e., $10^{-4\sim}$ 5×10^{-3} [59]. The thickening strain, $\varepsilon_t^{Al_2O_3}$, is usually considered as 10 times the lateral strain [12,65]. Thus, in the present work, the values of $\varepsilon_l^{Al_2O_3}$ and $\varepsilon_t^{Al_2O_3}$ are selected as 2×10^{-3} and 2×10^{-2}, respectively. Similarly, the MO formation can be represented by the following reaction.

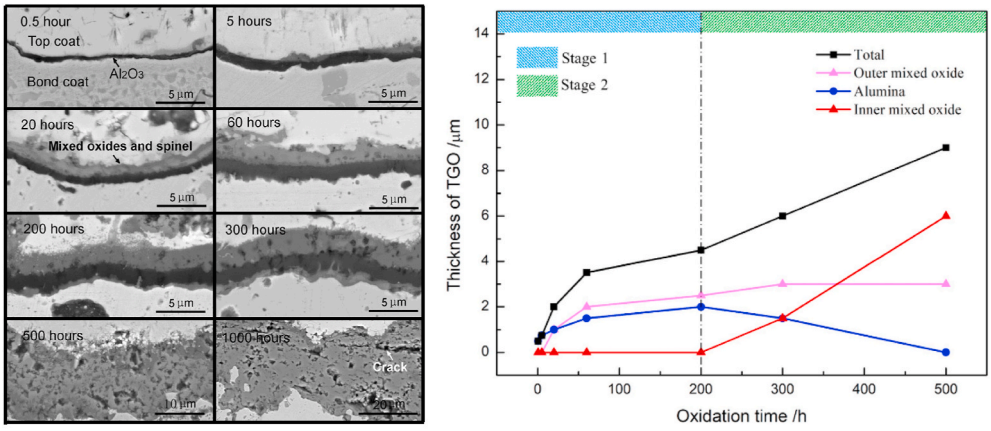

Fig. 1. (a) Backscattered electron images of cross-sectional morphology of TGO layer at different oxidation times; (b) evolution of TGO thickness at thermal oxidation [54].

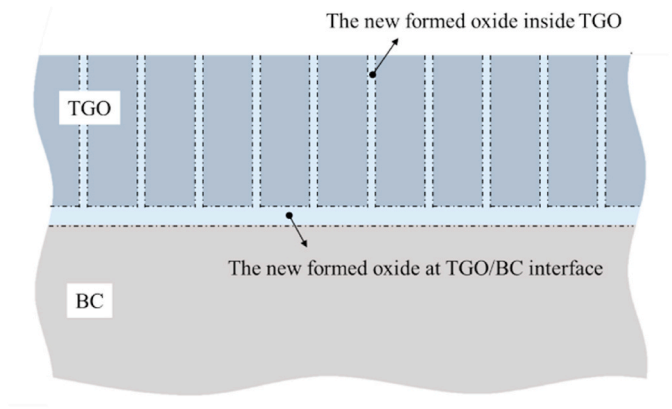

Fig. 2. Schematic of TGO growth in the TBC system. Oxides form at TGO–BC interface and within the columnar TGO, inducing a thickening growth strain (ε_t) and lateral growth strain (ε_l), respectively.

$$[Ni] + \alpha - Al_2O_3 + Cr_2O_3 + [O] \rightarrow Ni(Al, Cr)_2O_4 \quad (2)$$

Although the magnitude of the strain induced by this reaction has not been reported in the literature, a qualitative estimation has been recently provided by Maier et al. [58]; They indicated that the strain associated with the MO formation was isotropic and several times larger than that of Al_2O_3. Accordingly, it is assumed that the thickening and lateral strains caused by the MO growth are identical and equal to 4×10^{-2} (i.e., $\varepsilon_l^{MO} = \varepsilon_t^{MO} = \varepsilon^{MO} = 4 \times 10^{-2}$).

The implementation of TGO growth into the FE model is schematically shown in Fig. 3. In the first stage (i.e., 0–200 h), the outer MO and dense alumina grow simultaneously, and in the second stage (after 200 h), the inner MO begins to form at the bottom and gradually replace the initially formed alumina. In the proposed model, it is assumed that the transitioning of the 'phase' from the bond coat to alumina and from alumina to MO consistently occurs over time as the oxidation progresses. To define these transitions, the user subroutines USDFLD and UEXPAN in the commercial FEM package, ABAQUS 6.14, are utilized. All the field variables of elements, such as material properties and thermal growth strains, can be defined as a function of a solution-dependent variable (SDV). This state variable (SDV) defines the various types of oxides as well as the element phase transition in which 0, 1, and 2 represent the bond coat, alumina, and MO, respectively. The changes in the SDV with the oxidation time, from 0 to 1 and then from 1 to 2, exactly follow the variation in the thickness of different components in the TBC system, as shown in Fig. 1(b). The oxidation generates the thickening and lateral growth strains within the columnar TGO grain. Baker et al. [71] proved that the TGO growth strain should be implemented on the elements at the TGO–BC interface; this can be easily achieved by exploiting the UEXPAN subroutine.

To illustrate the 'phase' transitions upon thermal oxidation, an FE analysis flowchart of the ninth TGO element layer, which is located 4–4.5 μm in the TGO, is shown in Fig. 4; T_{total} and Δt denotes the total exposure and increment times, respectively. When the exposure time is less than 60 h, the material of the ninth element layer lies in the initial bond coat; thus, no growth strain is involved. From 60 to 200 h, the bond coat at that location starts to oxidize, and $\alpha - Al_2O_3$ is first generated, accompanied by the corresponding growth strain. From 200 to 300 h, this layer remains as $\alpha - Al_2O_3$. After 300 h, the inner MO begins to form and expand, gradually replacing the initial alumina layer. The material property transforms from that of $\alpha - Al_2O_3$ to that of MO; the growth strain of MO is applied to this element layer. A similar procedure is also applied to other TGO discretized layers.

2.2. Geometry and material properties

Previous research works have demonstrated that high growth stresses, which lead to the failure of TBC systems, tend to accumulate in regions with curved interfaces [72]. The present work aims to analyze the complicated stress distribution in these ragged regions; accordingly, a two-dimensional plane strain model with a curved TC–TGO interface is developed, as shown in Fig. 5. The model consists of four different constituent layers representing the TC, TGO, BC, and substrate. To significantly reduce the influence of boundary conditions, the width of the TBC system is set as six times larger than that of the ragged region. A periodic boundary condition is imposed on both sides of the TBC model to ensure the compatibility of deformation; all geometric data are listed in Table 1. The meshes in the ragged region where 18 layers of elements are used for the initial TGO and TGO thickening layer (each layer has a TGO thickness of 0.5 μm) are refined. After meshing, the resulting model consists of 148 312 four-node quadrilateral elements. By checking the mesh sensitivity, it was confirmed that a good mesh-independent solution was obtained under this mesh refinement.

The material properties of the TBC system are listed in Table 1 [59, 73]. All layers are considered homogeneous and isotropic. The YSZ and substrate are assumed to follow the linear elastic constitutive law. For the TGO (alumina and MO) and BC layer, the following Norton power-law creep behavior is used:

$$\dot{\varepsilon_{cr}} = B\sigma^n \quad (3)$$

where $\dot{\varepsilon_{cr}}$ is the strain rate (s^{-1}), B is the pre-factor ($s^{-1}MPa^{-n}$), σ is the stress (MPa), and n is the power-law creep exponent. The creep indices

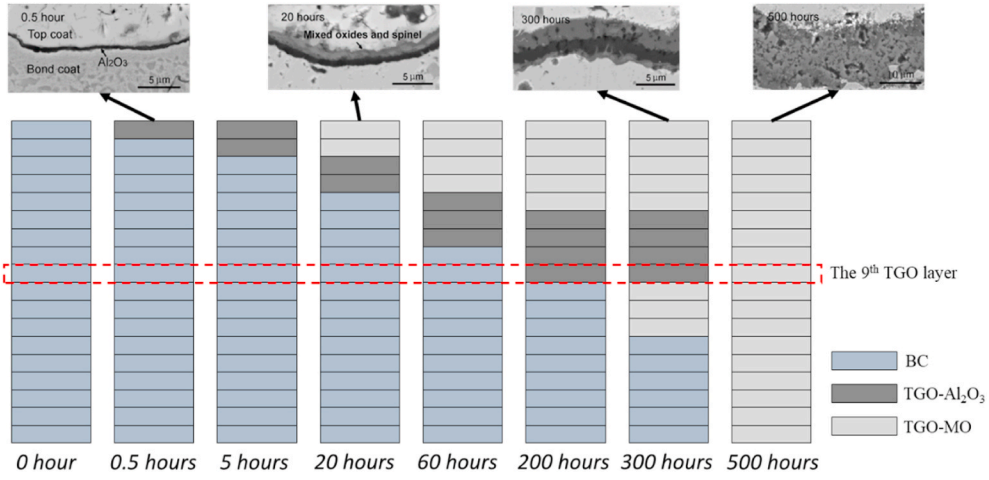

Fig. 3. Schematic of TGO growth process at different oxidation times.

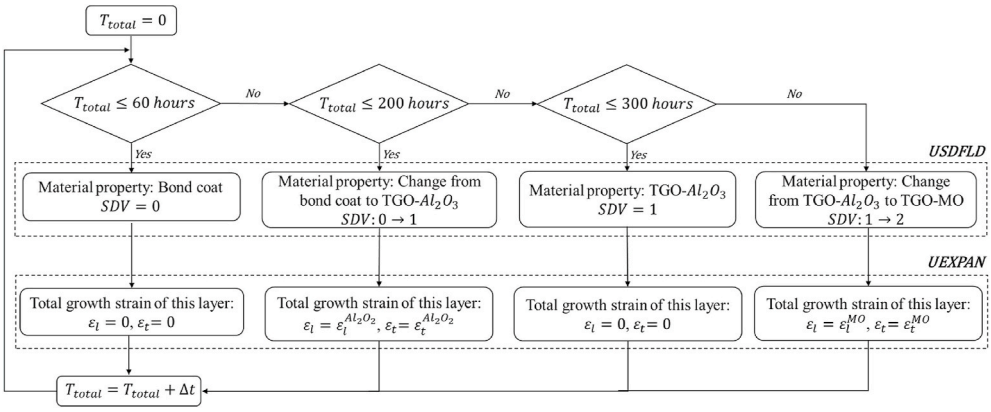

Fig. 4. Flowchart of FE analysis with user subroutines UEXPAN and USDFLD.

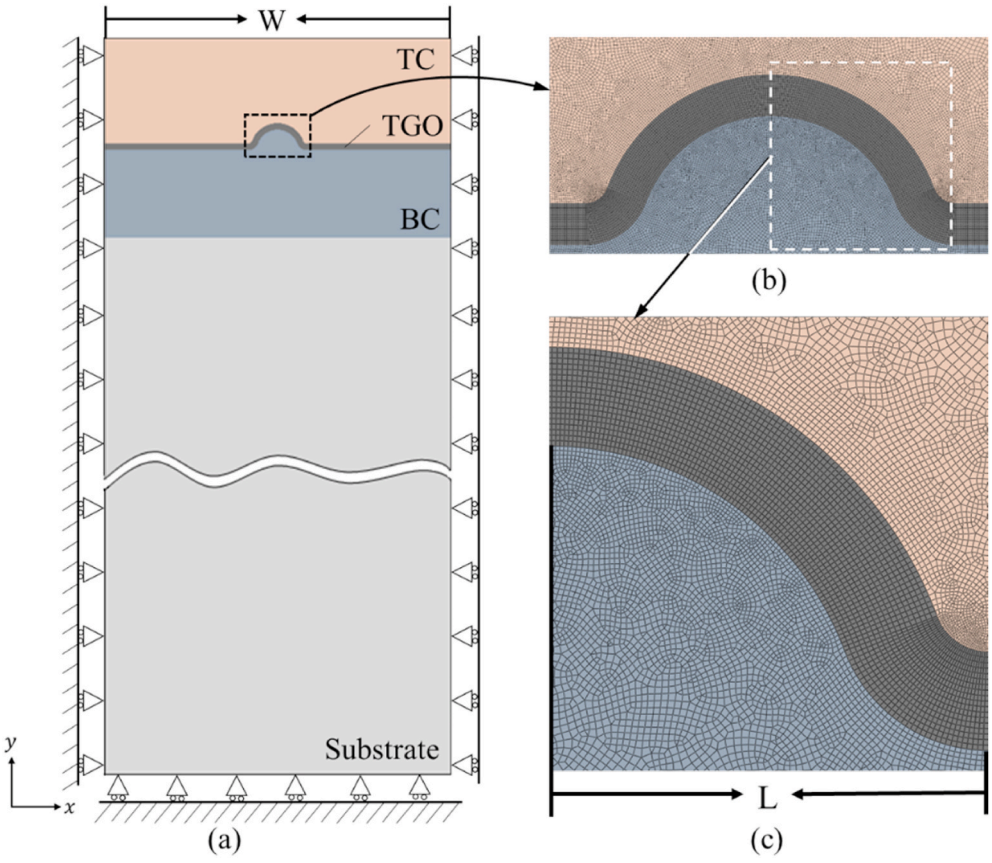

Fig. 5. (a) Schematic of two-dimensional model of the TBC system. (b) Refined mesh in ragged region vicinity; (c) Magnified view of refined mesh.

of each layer are summarised in Table 2; for BC, $B_{BC} = 3.9 \times 10^{-6}$ and $n_{BC} = 2.5$ [63]. For the TGO, three different orders of pre-factor are selected: large creep with $B_{Al_2O_3} = 7.3 \times 10^{-9}$ and $B_{MO} = 5 \times 10^{-9}$; medium creep with $B_{Al_2O_3} = 7.3 \times 10^{-10}$ and $B_{MO} = 5 \times 10^{-10}$; small creep with $B_{Al_2O_3} = 7.3 \times 10^{-11}$ and $B_{MO} = 5 \times 10^{-11}$. The effect of TGO creep, which is a key factor in determining the stress field and TBC failure, can be investigated by comparing the results from the three simulation cases. The power-law creep exponent is fixed as $n_{Al_2O_3} = n_{MO} = 1$ [59,64,73].

The temperature loading history consists of two stages. First, the TBC system is held at 1100 °C for 500 h (holding time, t_H), representing its service situation in a high-temperature environment. Then, the model is exposed to a temperature gradient decreasing from 1100 to 25 °C for 1 h (cooling time, t_L). In this work, the growth stress induced by the oxidation during the holding time and the mismatch stress induced by the different coefficients of thermal expansion (CTE) during the cooling time [fx]are investigated. At a high temperature in a stress-free state, the TBC system is sprayed. Moreover, the heating stage is not considered in the present simulation. Similar assumptions have also been used in other studies [34,35,46,70,74–76].

3. Results and discussions

TBC in heavy-duty gas turbines usually serves at high temperature for months, then it cools down along with the halt of the engine for maintenance. Based on the generalized numerical framework and the new model, we investigate the stress evolution with the TGO growth for

Table 1
Physical and geometric parameters*.

	Temperature (°C)	Young's modulus (GPa)	Poisson's ratio	Yield strength (MPa)	Thermal expansion ($\alpha \times 10^{-6}/°C$)	Layer thickness (μm)
TC	25	50	0.1	/	9.0	200
	200				9.2	
	400				9.6	
	800				10.8	
	1100				12.2	
TGO ($\alpha - Al_2O_3$)	/	325	0.3	/	8	0.5 (Initial)
TGO (Mixed oxide)	/	100	0.3	/	6	0 (Initial)
BC	25	200	0.3	426	12.3	150
	200	190		412	14.2	
	400	175		396	15.2	
	800	145		284	16.3	
	1100	120		114	17.6	
SUB	25	220	0.3	/	14.8	1500
	200	210			15.2	
	400	190			15.6	
	800	155			16.9	
	1100	120			18.0	

$*W = 480\mu m$, $L = 40\mu m$. The parameters of $\alpha - Al_2O_3$ and mixed oxide is taken from Ref. [59] and other material date are taken from Ref. [73].

Table 2
Creep parameters [59,63,64,73].

	B ($s^{-1}MPa^{-n}$)		n
BC	3.9×10^{-6}		2.5
TGO ($\alpha - Al_2O_3$)	Large creep:	7.3×10^{-9}	1
	Medium creep:	7.3×10^{-10}	
	Small creep:	7.3×10^{-11}	
TGO (Mixed oxide)	Large creep:	5×10^{-9}	1
	Medium creep:	5×10^{-10}	
	Small creep:	5×10^{-11}	

the two circumstances.

3.1. Stress development during high-temperature oxidation

In order to highlight the influence of inner MO growth. Two cases are investigated: Case A describes a completed oxidation process extracted from the experimental observation, which includes two oxidation stages. While in Case B, only the first stage of oxidation is considered, i.e. the formation of inner MO in the second stage is ignored. Similar simplified models of the TGO growth, such as case B, have been widely used in most of the previous studies [59,61,62,70]. Although the foregoing models may be useful to qualitatively capture the stress evolution induced by the TGO growth, the quantitative predictions of the stress field from the simplified models can substantially differ from those of the more realistic TGO growth model with two stages of oxidation.

The thickness and distribution of different components within the TBC system at different exposure times for Cases A and B are plotted in Fig. 6, (a) and (b), respectively. Different components are represented by the contour plot of the SDV: the black regions (SDV = 1) represent the alumina layer developed upon the early oxidation, whereas the dark grey regions (SDV = 2) represent the MO layers generated in the following oxidation process. During the first stage of oxidation (0–200 h), alumina and outer MO were simultaneously formed, and no difference between Cases A and B was found. However, after 200 h, the inner MO began to form and gradually replaced the initially formed alumina layer in Case A. The evolution of the thickness and composition of different oxide components in Case A is in good agreement with experimental observations, as shown in Fig. 1, indicating that the modified TGO growth model can well represent the real TGO growth process. In contrast, as shown in Fig. 6(b), no formation and growth of the inner MO are observed in Case B.

The growth strain associated with the MO formation is several times larger than that of Al_2O_3. The growth of the inner MO layer and the subsequent replacement of Al_2O_3 simulated in case A would induce a significant difference in the distribution of growth stresses when compared with the simplified case (Case B). The stress evolutions with and without considering the two stages of oxidation in the TBC system are plotted in Fig. 7. The maximum σ_{yy} stress within the TC layer is selected to represent the characteristic stress level because it is usually the direct cause of the TC protective layer spalling, which occurs during the service life of the TBC system. The σ_{yy} stress distributions within the TC layer at 20, 200, and 500 h are also shown in the insets of Fig. 7. In

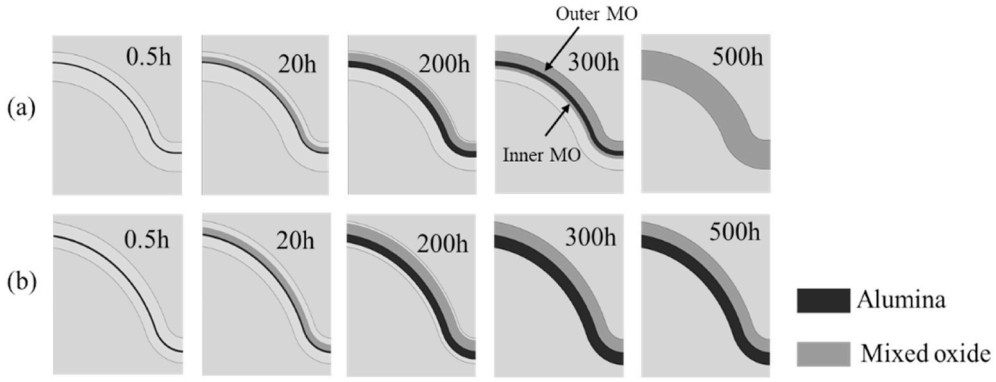

Fig. 6. Contour plot of SDV representing thickness and distribution of different oxides within the TBC system at different exposure times. (a) Case A: TGO growth with two stages of oxidation; (b) Case B: TGO growth only with the first stage of oxidation.

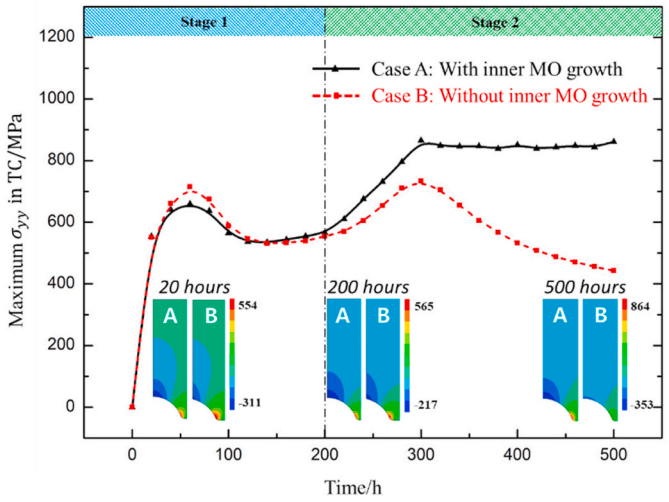

Fig. 7. Evolution of maximum σ_{yy} stress within TC layer with (Case A) and without (Case B) considering two stages of oxidation in the TBC system. Insets show distributions of σ_{yy} within TC layer at 20, 200, and 500 h upon high-temperature oxidation.

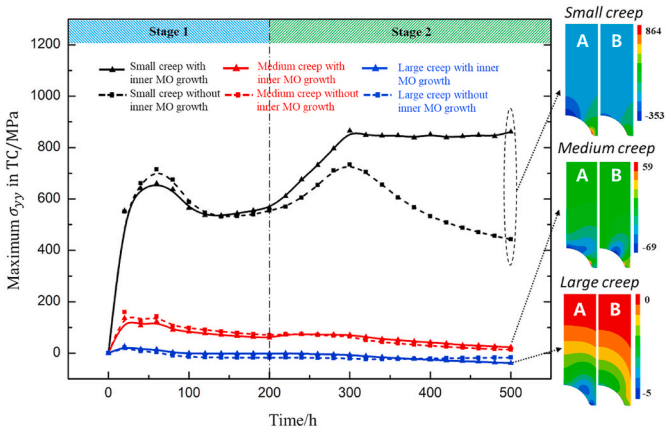

Fig. 8. Evolution of maximum σ_{yy} stress within TC layer upon thermal oxidation at different creep rates of TGO layer. Insets show distributions of σ_{yy} within TC layer at 500 h upon high-temperature oxidation.

this study, to minimize the influence of stress relaxation, the small creep pre-factors of the BC and TGO layers are preset.

In Fig. 7, the maximum value and distribution of σ_{yy}in the TC layer before 200 h for Cases A and B are practically identical because they have the same TGO growth behaviors in the first stage of oxidation. In the second stage of oxidation, the Al_2O_3 and outer MO layers continue to thicken, whereas the inner MO layer starts to form and replace the initially formed Al_2O_3 layer. From 200 to 300 h, the growths of Al_2O_3 and outer MO layers dominate the oxidation of the BC layer, resulting in the continuous increase in magnitudes of σ_{yy} in the TC layer. With the contribution of the inner MO layer growth, the increase in σ_{yy} in Case A is slightly greater than that in Case B, which does not consider the inner MO layer growth. After 300 h, the formation of Al_2O_3 and outer MO layers is practically complete. Eventually, the formation of the inner MO layer dominates the oxidation of the BC layer; this MO layer then replaces the initially formed Al_2O_3 layer, as shown in Fig. 6(a). This second stage of oxidation causes the TC layer to maintain a relatively high-stress level of approximately 860 MPa, as shown in Fig. 7. In contrast, as indicated by Fig. 6(b), the thickness and distribution of the various oxide components of TGO remain unchanged after 300 h, leading to the stress relaxation from 700 to 440 MPa. A previous study confirmed that the maximum σ_{yy} stress located at the flank of the protuberance generated short subcritical cracks within the TC layer; ultimately, these cracks resulted in the catastrophic spalling of this layer [72]. Under these circumstances, it is assumed that the new TGO growth model in this work, which considers the two stages of TGO growth, can better predict the stress field within the TBC system and system failure; that is, the high-stress level caused by the growth of the inner MO layer promotes the failure of the TBC system.

The effect of TGO layer creep is also considered in the present work. The TBC system usually functions in an extremely high-temperature environment in which the stress relaxation caused by the creep of the superalloy cannot be ignored. Moreover, the TGO layer creep rate varies over several orders at a high temperature gradient. Therefore, a qualitative study of the relationship between the stress field developed within the TBC system and the creep behavior of the TGO layer is crucial. The distribution and evolution of the maximum σ_{yy} stress within the TC layer upon thermal oxidation at different creep rates are shown in Fig. 8. Three different pre-factor orders for the TGO layer are selected to represent different creep rates, i.e., large creep with $B_{Al_2O_3} = 7.3\times 10^{-9}$ and $B_{MO} = 5\times 10^{-9}$, medium creep with $B_{Al_2O_3} = 7.3\times 10^{-10}$ and $B_{MO} = 5\times 10^{-10}$, and small creep with $B_{Al_2O_3} = 7.3\times 10^{-11}$ and $B_{MO} = 5\times 10^{-11}$. It is found that the σ_{yy} stress within the TC layer induced by the TGO growth is significantly relaxed as the creep rate increases. For the case of a small creep with an inner MO growth (black solid lines), the maximum σ_{yy} stress within the TC layer (usually developed at the valley of the protuberance) always maintains a relatively high level and reaches ~800 MPa after 500 h of oxidation. This indicates that the stress relaxation induced by the small creep rate is a relatively slow process compared with the development of stress generated by the TGO growth; consequently, a high growth stress, which is maintained within the TC layer, presumably causes the initiation and propagation of sub-cracks. In contrast, for the case of the large creep with the inner MO growth, the thermal growth stresses completely relax as a result of the relatively fast TGO creep, as shown by the blue solid lines in Fig. 8. In this circumstance, the TC layer in the TBC system is under a stress-free state despite the continuous TGO growth.

The isothermal oxidation at high temperatures also leads to the development of normal stress (σ_n) at the TGO–TC and TGO–BC interfaces, potentially resulting in the delamination of the TC or TGO layer. The distributions of normal stress (σ_n) as a function of the normalized location at the TGO–TC and TGO–BC interfaces are plotted in Fig. 9, (a) and (b), respectively. The normal stress distributions are obtained at the oxidation time of 500 h, at which point the oxidation of the BC layer is practically complete. At the TGO–TC interface, a compressive stress field develops at the peak of the protuberance and transforms into a tensile stress field at the valley. The transformation of the developed stress from compression to tension at the valley mainly results from the change in the sign of the radius of curvature of the TGO–TC interface [63]. It should be noted that the inner MO growth increases the magnitudes of the compressive stress at the peak and tensile stress at the valley; the comparison between the solid and dashed lines is shown in Fig. 9(a). This comparison indicates that the growth of the inner MO layer not only increases the possibility of coating layer spalling but also the facilitation of interfacial failures, such as interfacial delamination, by inducing a larger normal stress field at the interface. However, in Fig. 9(b), the plots of the normal stress distributions (σ_n) at the TGO–BC interface indicates that the growth of the inner MO does not simply increase the compressive stress at the peak and tensile stress at the valley but also enhances the compressive normal stress at the interface while reducing the tensile stress. However, this does not imply that the inner MO growth reduces the possibility of interfacial delamination at the TGO–BC interface. It should be noted that once the alumina layer is gradually replaced by the inner MO, the interfacial fracture toughness of the TGO–BC interface significantly weakens. Therefore, even if the tensile normal stress that developed at the interface slightly

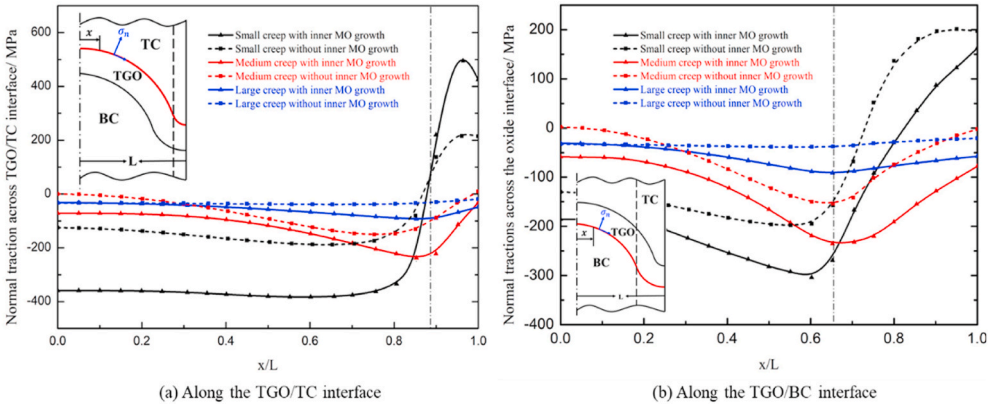

Fig. 9. Normal traction (σ_n) at (a) TGO–TC and (b) TGO–BC interfaces at 500 h with high-temperature oxidation.

decreases, the interfacial delamination still occurs because of the weak interfacial strength.

Similar to the σ_{yy} variation in the TC layer with various creep coefficients of the TGO layer, the normal stress generated by the small TGO creep at the interface is significantly higher than those induced by the medium and large creeps, as shown in Fig. 7. Moreover, the large TGO creep reduces the stresses induced by growth. In Fig. 9, (a) and (b), it is clear that the tensile normal stress at the valley only appears at a low creep rate, indicating that if the stress induced by growth is relaxed by the creep, the normal stress at the interface tends to be compressive. Although it is difficult to experimentally measure the TGO layer creep rate, this qualitative study still provides a good prediction of the stress evolution and possibility of TBC failure.

3.2. Stress development after cooling

Stress development during the cooling stage is another critical factor that influences the mechanical integrity of the TBC system. During the cooling stage, the temperature decreases from 1100 to 25 °C, as discussed in Section 2.2. The TBC system would generate another stress field because of the CTE mismatch. In this study, because the cooling time is relatively short, the creep during cooling is ignored. For the three different creep rates, the stress distributions (σ_{22}) within the TC layer after cooling are plotted in Fig. 10(a). It is evident that σ_{22} exhibits a similar distribution for both cases with and without considering the inner MO growth; it also exhibits different magnitudes, indicating that the inner MO growth increases the stress level. Again, the TGO layer creep affects the distribution of mismatch stress. However, it does not considerably relax the stress during cooling because of the relatively short cooling time compared with the oxidation time. Nevertheless, the creep strain that is generated during the high-temperature oxidation alters the mismatch strain and stress resulting from the CTE mismatch during cooling, as shown in Fig. 10(a). The maximum σ_{22} stress in Fig. 10(a), normalized by the Young's modules of TC, is plotted as a histogram in Fig. 10(b). Compared with the stress evolution with high-temperature oxidation, as discussed in Section 3.1, the effect of inner MO growth on the stress evolution upon cooling is not limited to the low creep rate; instead, the inner MO growth increases the stress magnitude

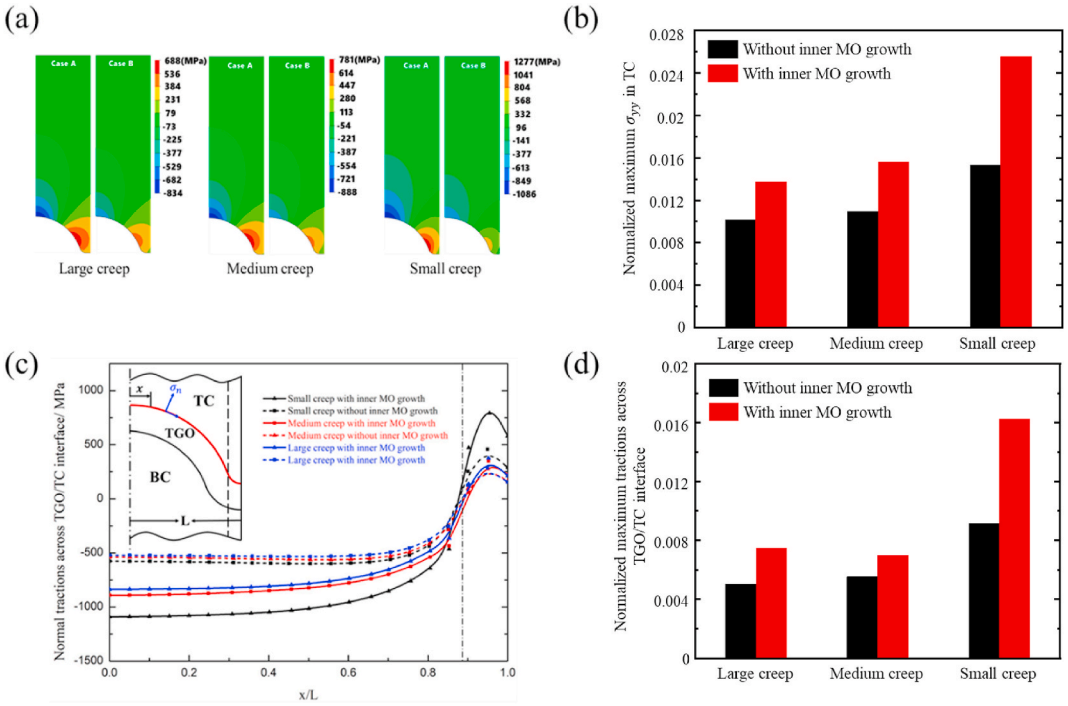

Fig. 10. (a) Distributions of σ_{yy} within TC layer after cooling; (b) The normalized maximum σ_{yy} stress within TC after cooling; (c) Distribution of normal stress (σ_n) developed at TGO–TC interface after cooling; (d) The normalized maximum tractions (σ_n) developed at TGO–TC interface after cooling.

with the creep rate. This indicates that the oxidation of the inner MO significantly affects the stress distribution and failure after cooling.

The normal stress distribution (σ_n) at the TGO–TC interface after cooling is plotted in Fig. 10(c). It can be observed that the inner MO growth distinctly increases the normal stress at the interface with the three creep rates. The maximum tensile stress at the valley shown in Fig. 10(c) is extracted and then plotted as a histogram in Fig. 10(d). The value of the maximum traction is also normalized by the Young's modules of TC. The inner MO growth increases the maximum tensile stress at the interface similar to its effect on the maximum normal stress (σ_{22}) within the TC layer. It significantly increases the possibility of interfacial delamination of the TC layer during cooling.

It is worth noting that the calculated stress may be much higher than some of the experimental measurement. This inconsistency can be due to several factors. Firstly, every material used here is assumed dense, consistent and homogeneous. The porosity and inhomogeneity of each components are not considered. Therefore, the strength of the material is stronger than that of the real situation. Secondly, this study does not engage the mechanism of crack's initiation and propagation, which can help reduce the stress level under real service conditions. Thirdly, the creep during cooling is not considered. So that the stress relaxation is neglected. Overall, the result of this study provides the maximum possible stress. Despite all this, the findings clearly indicate that the inner MO growth can dramatically intensify the low-temperature stresses. Thus, the inner MO growth may become the main reason for the failure of the TBC system during the shut down of heavy-duty gas turbines. To avoid this situation, several measures can be considered. For example, improve the powder formula to control the ingredient of MO, making the MO more uniform and have a smaller volume expansion rate. The thermal mismatch stress can also be moderated by a prolonged cooling stage, letting the stress have enough time to relax. In general, the modified TGO growth model with two stages of oxidation is essential for the analysis of stress development and can further provide a better approach for the failure analysis and service life prediction of the TBC system.

4. Conclusion

A numerical method is introduced to simulate the TGO growth and the stress evolution in the TBC system. A new TGO-growth model is formulated by considering the two-stage oxidation: In the first stage, the outer MO and alumina grow simultaneously. In the second stage, the inner MO forms at the bottom and gradually replace the alumina. The focus of this work is to study the second stage's effect, i.e. the inner MO growth. The stress evolutions, both in high-temperature oxidation and after cooling down, are studied.

By comparing the result with and without the inner MO growth, we found that the formation of the inner MO and its replacement of the initially formed alumina generate considerably higher stresses within the TBC system. During the high-temperature oxidation, the TGO creep can reduce the growth stress and decreases the adverse effect of the inner MO growth. However, the strain caused by inner MO growth is always present. Consequently, at the rapid cooling stage, the thermal mismatch stresses with inner MO growth is significantly higher than that without inner MO growth. Thus, the inner MO growth on the stress development in the TBC system is crucial to the failure of TBC systems. Our two-stage oxide growth model provides a better approach to accurately predict the service life of the TBC system.

Declaration of competing interest

The authors declare that they have no known competing financial interests or personal relationships that could have appeared to influence the work reported in this paper.

Acknowledgements

This work was supported by NSFC (11772246,11902240,11972025), the fund of State Key Laboratory of Long-life High Temperature Materials.

References

[1] A.G. Evans, D.R. Mumm, J.W. Hutchinson, G.H. Meier, F.S. Pettit, Mechanisms controlling the durability of thermal barrier coatings, Prog. Mater. Sci. 46 (2001) 505–553.
[2] W.J. Brindley, Thermal barrier coatings, J. Therm. Spray Technol. 5 (1996) 379–380.
[3] E. Garcia, P. Miranzo, R. Soltani, T.W. Coyle, Microstructure and thermal behavior of thermal barrier coatings, J. Therm. Spray Technol. 17 (2008) 478–485.
[4] Q. Zhang, C.J. Li, Y. Li, S.L. Zhang, X.R. Wang, G.J. Yang, C.X. Li, Thermal failure of nanostructured thermal barrier coatings with cold-sprayed nanostructured NiCrAlY bond coat, J. Therm. Spray Technol. (2008) 838–845.
[5] D. Balevic, S. Hartman, R. Youmans, Heavy-duty Gas Turbine Operating and Maintenance Considerations, GE Energy, Atlanta, GA, 2010.
[6] C.H. Hsueh, E.R. Fuller, Analytical modeling of oxide thickness effects on residual stresses in thermal barrier coatings, Scripta Mater. 42 (2000) 781–787.
[7] F. Tang, J.M. Schoenung, Local accumulation of thermally grown oxide in plasma-sprayed thermal barrier coatings with rough top-coat/bond-coat interfaces, Scripta Mater. 52 (2005) 905–909.
[8] A. Rabiei, A.G. Evans, Failure mechanisms associated with the thermally grown oxide in plasma-sprayed thermal barrier coatings, Acta Mater. 48 (2000) 3963–3976.
[9] W.K. Schlichting, N.P. Padture, E.H. Jordan, M. Gell, Failure modes in plasma-sprayed thermal barrier coatings, Mater. Sci. Eng. 342 (2003) 120–130.
[10] K. Bouhanek, O.A. Adesanya, F.H. Stott, P. Skeldon, D.G. Lees, G.C. Wood, High-temperature Oxidation of Thermal Barrier Coating Systems on RR3000 Substrates: Pt Aluminide Bond Coats, Trans Tech Pub, 2001, pp. 615–622.
[11] V.K. Tolpygo, D.R. Clarke, K.S. Murphy, Oxidation-induced failure of EB-PVD thermal barrier coatings, Surf. Coating. Technol. 146 (2001) 124–131.
[12] D.R. Mumm, A.G. Evans, I.T. Spitsberg, Characterization of a cyclic displacement instability for a thermally grown oxide in a thermal barrier system, Acta Mater. 49 (2001) 2329–2340.
[13] N.P. Padture, M. Gell, E.H. Jordan, Thermal barrier coatings for gas-turbine engine applications, Science 296 (2002) 280–284.
[14] E.P. Busso, L. Wright, H.E. Evans, L.N. McCartney, S.R.J. Saunders, S. Osgerby, J. Nunn, A physics-based life prediction methodology for thermal barrier coating systems, Acta Mater. 55 (2007) 1491–1503.
[15] N.M. Yanar, F.S. Pettit, G.H. Meier, Failure characteristics during cyclic oxidation of yttria stabilized zirconia thermal barrier coatings deposited via electron beam physical vapor deposition on platinum aluminide and on NiCoCrAlY bond coats with processing modifications for improved performance, Metall. Mater. Trans. 37 (2006) 1563–1580.
[16] W.R. Chen, R. Archer, X. Huang, B.R. Marple, TGO growth and crack propagation in a thermal barrier coating, J. Therm. Spray Technol. (2008) 858–864.
[17] C.G. Levi, E. Sommer, S.G. Terry, A. Catanoiu, M. Rühle, Alumina grown during deposition of thermal barrier coatings on NiCrAlY, J. Am. Ceram. Soc. 86 (2003) 676–685.
[18] W.R. Chen, X. Wu, B.R. Marple, D.R. Nagy, P.C. Patnaik, TGO growth behaviour in TBCs with APS and HVOF bond coats, Surf. Coating. Technol. 202 (2008) 2677–2683.
[19] Q. Chen, W.G. Mao, Y.C. Zhou, C. Lu, Effect of Young's modulus evolution on residual stress measurement of thermal barrier coatings by X-ray diffraction, Appl. Surf. Sci. 256 (2010).
[20] R.J. Christensen, D.M. Lipkin, D.R. Clarke, K. Murphy, Nondestructive evaluation of the oxidation stresses through thermal barrier coatings using Cr3+ piezospectroscopy, Appl. Phys. Lett. 69 (1996) 3754–3756.
[21] P. Scardi, M. Leoni, L. Bertini, L. Bertamini, F. Cernuschi, Strain gradients in plasma-sprayed zirconia thermal barrier coatings, Surf. Coating. Technol. 108 (1998) 93–98.
[22] N.I. Baklanova, B.A. Kolesov, T.M. Zima, Raman study of yttria-stabilized zirconia interfacial coatings on Nicalon^{TM} fiber, J. Eur. Ceram. Soc. 27 (2007) 165–171.
[23] P. Scardi, M. Leoni, L. Bertini, L. Bertamini, Residual stress in partially stabilised-zirconia TBCs: experimental measurement and modelling, Surf. Coating. Technol. 94 (1997) 82–88.
[24] B.S. Yilbas, A.F.M. Arif, Residual stress analysis for hv of diamalloy 1005 coating on Ti–6Al–4V alloy, Surf. Coating. Technol. 202 (2007) 559–568.
[25] K.W. Schlichting, K. Vaidyanathan, Y.H. Sohn, E.H. Jordan, M. Gell, N.P. Padture, Application of Cr 3+ photoluminescence piezo-spectroscopy to plasma-sprayed thermal barrier coatings for residual stress measurement, Mater. Sci. Eng. 291 (2000) 68–77.
[26] B. Li, X. Fan, T. Wang, K. Zhou, Interfacial fracture behavior of double-ceramic-layer thermal barrier coating system with segmented structure, Eng. Fract. Mech. 201 (2018) 13–28.
[27] P. Prapamonthon, S. Yooyen, S. Sleesongsom, CHT/CFD analysis of thermal sensitivity of a transonic film-cooled guide vane, C. - Comput. Model. Eng. Sci. 119 (2019) 593–615.

[28] B. Li, X. Fan, K. Zhou, T. Wang, A semi-analytical model for predicting stress evolution in multilayer coating systems during thermal cycling, Int. J. Mech. Sci. 135 (2018) 31–42.
[29] B. Li, X. Fan, H. Okada, T. Wang, Mechanisms governing the failure modes of dense vertically cracked thermal barrier coatings, Eng. Fract. Mech. 189 (2018) 451–480.
[30] P. Jiang, X. Fan, Y. Sun, D. Li, B. Li, T. Wang, Competition mechanism of interfacial cracks in thermal barrier coating system, Mater. Des. 132 (2017) 559–566.
[31] R. Xu, X.L. Fan, W.X. Zhang, Y. Song, T.J. Wang, Effects of geometrical and material parameters of top and bond coats on the interfacial fracture in thermal barrier coating system, Mater. Des. 47 (2013) 566–574.
[32] W.X. Zhang, X.L. Fan, T.J. Wang, The surface cracking behavior in air plasma sprayed thermal barrier coating system incorporating interface roughness effect, Appl. Surf. Sci. 258 (2011) 811–817.
[33] X.L. Fan, R. Xu, W.X. Zhang, T.J. Wang, Effect of periodic surface cracks on the interfacial fracture of thermal barrier coating system, Appl. Surf. Sci. 258 (2012) 9816–9823.
[34] L. Chen, L. Yueming, Interface stress evolution considering the combined creep–plastic behavior in thermal barrier coatings, Mater. Des. 89 (2016) 245–254.
[35] M. Gupta, R. Eriksson, U. Sand, P. Nylén, A diffusion-based oxide layer growth model using real interface roughness in thermal barrier coatings for lifetime assessment, Surf. Coating. Technol. 271 (2015) 181–191.
[36] E.P. Busso, Z.Q. Qian, M.P. Taylor, H.E. Evans, The influence of bondcoat and topcoat mechanical properties on stress development in thermal barrier coating systems, Acta Mater. 57 (2009) 2349–2361.
[37] B. Yan, C. Lim, Z. Song, L. Zhu, Analysis of polarization in realistic Li ion battery electrode microstructure using numerical simulation, Electrochim. Acta 185 (2015) 125–141.
[38] Q. Shen, L. Yang, Y.C. Zhou, Y.G. Wei, W. Zhu, Effects of growth stress in finite-deformation thermally grown oxide on failure mechanism of thermal barrier coatings, Mech. Mater. 114 (2017) 228–242.
[39] W. Xie, E. Jordan, M. Gell, Stress and cracking behavior of plasma sprayed thermal barrier coatings using an advanced constitutive model, Mater. Sci. Eng. 419 (2006) 50–58.
[40] J.T. DeMasi-Marcin, K.D. Sheffler, S. Bose, ASME Paper 89-GT-132, Am. Soc. Mech. Eng., New York, 1989.
[41] R.A. Miller, C.E. Lowell, Failure mechanisms of thermal barrier coatings exposed to elevated temperatures, Thin Solid Films 95 (1982) 265–273.
[42] W.J. Brindley, Properties of plasma-sprayed bond coats, J. Therm. Spray Technol. 6 (1997) 85.
[43] G.J. Petrus, B.L. Ferguson, A software tool to design thermal barrier coatings: a technical note, J. Therm. Spray Technol. 6 (1997) 29–34.
[44] J. Jiang, B. Xu, W. Wang, R.A. Adjei, X. Zhao, Y. Liu, Finite element analysis of the effects of thermally grown oxide thickness and interface asperity on the cracking behavior between the thermally grown oxide and the bond coat, J. Eng. Gas Turbines Power 139 (2017) 22504.
[45] Q.M. Yu, H.L. Zhou, L.B. Wang, Influences of interface morphology and thermally grown oxide thickness on residual stress distribution in thermal barrier coating system, Ceram. Int. 42 (2016) 8338–8350.
[46] M. Gupta, K. Skogsberg, P. Nylén, Influence of topcoat–bondcoat interface roughness on stresses and lifetime in thermal barrier coatings, J. Therm. Spray Technol. 23 (2014) 170–181.
[47] J. Rösler, M. Bäker, K. Aufzug, A parametric study of the stress state of thermal barrier coatings: Part I: creep relaxation, Acta Mater. 52 (2004) 4809–4817.
[48] W.R. Chen, X. Wu, B.R. Marple, P.C. Patnaik, The growth and influence of thermally grown oxide in a thermal barrier coating, Surf. Coating. Technol. 201 (2006) 1074–1079.
[49] J.A. Haynes, E.D. Rigney, M.K. Ferber, W.D. Porter, Oxidation and degradation of a plasma-sprayed thermal barrier coating system, Surf. Coating. Technol. (1996) 86–87, 102–108.
[50] C.H. Lee, H.K. Kim, H.S. Choi, H.S. Ahn, Phase transformation and bond coat oxidation behavior of plasma-sprayed zirconia thermal barrier coating, Surf. Coating. Technol. 124 (2000) 1–12.
[51] L. Ajdelsztajn, J.A. Picas, G.E. Kim, F.L. Bastian, J. Schoenung, V. Provenzano, Oxidation behavior of HVOF sprayed nanocrystalline NiCrAlY powder, Mater. Sci. Eng. 338 (2002) 33–43.
[52] E.A.G. Shillington, D.R. Clarke, Spalling failure of a thermal barrier coating associated with aluminum depletion in the bond-coat, Acta Mater. 47 (1999) 1297–1305.
[53] P. Niranatlumpong, C.B. Ponton, H.E. Evans, The failure of protective oxides on plasma-sprayed {NiCoCrAlY} overlay coatings, Oxid. Metals 53 (2000) 241–258.
[54] Y. Bai, C. Ding, H. Li, Z. Han, B. Ding, T. Wang, L. Yu, Isothermal oxidation behavior of supersonic atmospheric plasma-sprayed thermal barrier coating system, J. Therm. Spray Technol. 22 (2013) 1201–1209.
[55] W.R. Chen, X. Wu, B.R. Marple, P.C. Patnaik, Oxidation and crack nucleation/growth in an air-plasma-sprayed thermal barrier coating with NiCrAlY bond coat, Surf. Coating. Technol. 197 (2005) 109–115.
[56] W.R. Chen, X. Wu, B.R. Marple, R.S. Lima, P.C. Patnaik, Pre-oxidation and TGO growth behaviour of an air-plasma-sprayed thermal barrier coating, Surf. Coating. Technol. 202 (2008) 3787–3796.
[57] Z. Chen, F. Yuan, Z. Wang, S. Zhu, The oxide scale formation and evolution on detonation gun sprayed NiCrAlY coatings during isothermal oxidation, Mater. Trans. 48 (2007) 2695–2702.
[58] R.D. Maier, C.M. Scheuermann, C.W. Andrews, Degradation of a two-layer thermal barrier coating under thermal cycling, Am. Ceram. Soc. Bull. 60 (1981) 555–560.
[59] R. Xu, X.L. Fan, W.X. Zhang, T.J. Wang, Interfacial fracture mechanism associated with mixed oxides growth in thermal barrier coating system, Surf. Coating. Technol. 253 (2014) 139–147.
[60] B. Lv, H. Xie, R. Xu, X. Fan, W. Zhang, T.J. Wang, Effects of sintering and mixed oxide growth on the interface cracking of air-plasma-sprayed thermal barrier coating system at high temperature, Appl. Surf. Sci. 360 (2016) 461–469.
[61] E.P. Busso, H.E. Evans, Z.Q. Qian, M.P. Taylor, Effects of breakaway oxidation on local stresses in thermal barrier coatings, Acta Mater. 58 (2010) 1242–1251.
[62] F. Xie, Y. Sun, D. Li, Y. Bai, W. Zhang, Modelling of catastrophic stress development due to mixed oxide growth in thermal barrier coatings, Ceram. Int. 45 (2019) 11353–11361.
[63] A.M. Freborg, B.L. Ferguson, W.J. Brindley, G.J. Petrus, Modeling oxidation-induced stresses in thermal barrier coatings, Mater. Sci. Eng. 245 (1998) 182–190.
[64] M. Ranjbar-Far, J. Absi, G. Mariaux, D.S. Smith, Crack propagation modeling on the interfaces of thermal barrier coating system with different thickness of the oxide layer and different interface morphologies, Mater. Des. 32 (2011) 4961–4969.
[65] A.M. Karlsson, A.G. Evans, A numerical model for the cyclic instability of thermally grown oxides in thermal barrier systems, Acta Mater. 49 (2001) 1793–1804.
[66] M.T. Hernandez, A.M. Karlsson, M. Bartsch, On TGO creep and the initiation of a class of fatigue cracks in thermal barrier coatings, Surf. Coating. Technol. 203 (2009) 3549–3558.
[67] M. Białas, Finite element analysis of stress distribution in thermal barrier coatings, Surf. Coating. Technol. 202 (2008) 6002–6010.
[68] A. Saillard, M. Cherkaoui, L. Capolungo, E.P. Busso, Stress influence on high-temperature oxide scale growth: modeling and investigation on a thermal barrier coating system, Philos. Mag. A 90 (2010) 2651–2676.
[69] E.P. Busso, J. Lin, S. Sakurai, M. Nakayama, A mechanistic study of oxidation-induced degradation in a plasma-sprayed thermal barrier coating system.: Part I: model formulation, Acta Mater. 49 (2001) 1515–1528.
[70] L.Y. Ni, C. Liu, H. Huang, C.G. Zhou, Thermal cycling behavior of thermal barrier coatings with HVOF NiCrAlY bond coat, J. Therm. Spray Technol. 20 (2011) 1133–1138.
[71] M. Bäker, Influence of material models on the stress state in thermal barrier coating simulations, Surf. Coating. Technol. 240 (2014) 301–310.
[72] C.H. Hsueh, J.A. Haynes, M.J. Lance, P.F. Becher, M.K. Ferber, E.R. Fuller, S. A. Langer, W.C. Carter, W.R. Cannon, Effects of interface roughness on residual stresses in thermal barrier coatings, J. Am. Ceram. Soc. 82 (1999) 1073–1075.
[73] L. Su, W. Zhang, Y. Sun, T.J. Wang, Effect of TGO creep on top-coat cracking induced by cyclic displacement instability in a thermal barrier coating system, Surf. Coating. Technol. 254 (2014) 410–417.
[74] H.X. Zhu, N.A. Fleck, A.C.F. Cocks, A.G. Evans, Numerical simulations of crack formation from pegs in thermal barrier systems with NiCoCrAlY bond coats, Mater. Sci. Eng. 404 (2005) 26–32.
[75] P. Seiler, M. Bäker, T. Beck, M. Schweda, J. Rösier, FEM simulation of TBC failure in a model system, J. Phys. Conf. Ser. 240 (1) (2010) 012069.
[76] M. Caliez, J.L. Chaboche, F. Feyel, S. Kruch, Numerical simulation of EBPVD thermal barrier coatings spallation, Acta Mater. 51 (2003) 1133–1141.